Composites Part B 176 (2019) 107338

Contents lists available at ScienceDirect

Composites Part B

journal homepage: www.elsevier.com/locate/compositesb

Effect of graphene liquid crystal on dielectric properties of polydimethylsiloxane nanocomposites

Zhuangzhuang Zhang [a], Jiaoxia Zhang [a,**], Shiyun Li [a], Jianping Liu [a], Mengyao Dong [b,c], Yingchun Li [d], Na Lu [e], Shuya Lei [a], Jijun Tang [a], Jincheng Fan [f], Zhanhu Guo [b,*]

[a] School of Materials Science and Engineering, Jiangsu University of Science and Technology, Zhenjiang, 212003, China
[b] Integrated Composites Laboratory (ICL), Department of Chemical & Biomolecular Engineering, University of Tennessee, Knoxville, TN, 37996, USA
[c] Key Laboratory of Materials Processing and Mold (Zhengzhou University), Ministry of Education, National Engineering Research Center for Advanced Polymer Processing Technology, Zhengzhou University, Zhengzhou, 450002, China
[d] School of Materials Science and Engineering, North University of China, Taiyuan, 030051, China
[e] Lyles School of Civil Engineering, School of Materials Engineering, Birck Nanotechnology Center, Purdue University, West Lafayette, IN, 47906, USA
[f] College of Materials Science and Engineering, Changsha University of Science and Technology, Changsha, 410114, China

ARTICLE INFO

Keywords:
Graphene
Liquid crystal
High-permittivity
Polymer-matrix composites

ABSTRACT

Graphene can form a liquid crystal phase due to its anisotropic flake characteristics, it shows great potential in the field of high dielectric composites. In this paper, the graphene oxide sheets are grafted onto copolymer to uniformly disperse and maintain the liquid crystal state in a non-polar solvent, then the modified graphene oxide liquid crystal is transferred to polydimethylsiloxane. Graphene/polydimethylsiloxane nanocomposites are obtained by high temperature reduction and curing reactions. When the filler content is 4 wt%, the permittivity increases by 800% compared to pure polydimethylsiloxane. Therefore, graphene liquid crystal can significantly improve the dielectric properties of the nanocomposites than ordinary graphene, which provides a new method for preparing high dielectric properties composites.

1. Introduction

Polymer-matrix composites have attracted great interests and received wide potential applications [1–8] due to their simple processing, good mechanical flexibility, low cost and good compatibility [9–17]. High-permittivity polymer-matrix composites have successfully replaced traditional high dielectric materials such as ceramics and metals [18–25], and have been widely used in supercapacitors, radar, aerospace, underwater navigation and mobile electronics, lasers, biomedical imaging and non-destructive testing [26–28]. In recent years, great progress has been made on high-permittivity polymer–matrix composites. The most popular method is to dope conductive particles into the polymers, thereby obtaining the high dielectric polymer composites with great application potentials [19,27]. There are many factors that affect the dielectric properties, such as the polymer chemical structure, the shape of filler and their amount in the composites, etc. The aspect ratio is introduced to describe the effect of the filler shape on the dielectric properties [18,20]. The rod-like fillers with a larger aspect ratio than the spherical particles are easier to form a conductive path when they are randomly oriented so that it is not suitable for preparing high dielectric properties composite [20]. However, the liquid crystal (LC) phase is difficult to form a conductive path because the layers are parallel to each other, and this is a method for obtaining composites of high dielectric properties [29].

Graphene was first obtained by micro-mechanical stripping method [30], and it is applied to many composites due to its outstanding performance in all aspects [31–35]. Since the graphene sheets have a high aspect ratio, the graphene-based composites have a low percolation threshold [36–40], and researchers often use them as conductive composites. But graphene has formed LC phases in aqueous solutions or polar organic solvents [41,42]. Therefore, graphene LC is very suitable to serve as a filler for high dielectric composites [20]. Usually, this method uses a surfactant stabilizer to prevent graphene sheets from coagulating and thus is harmful to the environment [43]. However, Yuan and co-worker have shown that the graphene sheets do not exhibit a low percolation threshold because nematic LC phases are formed

* Corresponding author.
** Corresponding author.
E-mail addresses: zhangjx@just.edu.cn (J. Zhang), zguo10@utk.edu (Z. Guo).

https://doi.org/10.1016/j.compositesb.2019.107338
Received 22 April 2019; Received in revised form 31 July 2019; Accepted 11 August 2019
Available online 12 August 2019
1359-8368/

before the graphene sheets reach the percolation threshold [29,44–46]. The orientation of the graphene sheets results in difficulty in forming conductive paths. Han and co-worker studied the effect of the thickness of the conductive nanosheet reduced graphene oxide (rGO) shell on the dielectric properties of the composites. It was found that the percolation threshold increased with the increase of the shell thickness [27]. This shows that the insulating shell can slow down the generation of conductive path, thus increases the permittivity of the composites. Therefore, graphene-based high dielectric composites can be obtained. Graphene does not spontaneously form a LC phase, but graphene oxide (GO) can spontaneously form nematic LC phases in a polar solvent, and it can also maintain a LC state in a polymer [47,48].

In this work, GO is dispersed in aqueous solution to form a LC phase, and then the graphene oxide liquid crystal (GOLC) sheet is graft-modified with polyaminopropylmethylsiloxane-b-polydimethylsiloxane (PAPMS-b-PDMS) copolymer to make it extraction to diethyl ether [49,50]. Therefore, the GOLC phases can be transferred to a non-polar organic solvent, and then transferred to polydimethylsiloxane (PDMS). High-temperature in situ thermal reductions of GO after volatilizing the organic solvent recovers the high conductivity of graphene [51–55], which is then solidified in the mold. By changing the contents of graphene, the composites can be obtained in a wide range of permittivity. PDMS is selected in this study since it has a high modulus of elasticity and is a constant value over a wide temperature range, which reduces the dielectric loss due to hysteresis. When the filler content is 4 wt%, the permittivity of liquid-crystalline graphene-based composites is increased by 800% compared to pure PDMS, and the loss tangent does not exceed 0.5. In addition, rGOLC/PDMS nanocomposites have high thermal stabilities.

2. Experimental

2.1. Preparation of GO

The GO was prepared by the modified Hummers' method [56]. First, graphite pre-oxidation experiment was carried out. Briefly, 5 g $K_2S_2O_8$ (China Sun Specialty Products Co., Ltd.), 5 g P_2O_5 (Shanghai Rich Joint Chemical Reagents Co., Ltd.), 20 mL H_2SO_4 (95–98% Shanghai Su Yi Chemical Reagent Co., Ltd.) and 10 g graphite powder (99% in purity, Ding Sheng Xin chemical industry Co., Ltd.) were placed in a beaker, and the temperature was raised to 80 °C to keep warm for 6 h and stirred constantly. Then it was washed with ultrapure water to close to neutral, and dried at 60 °C. Then graphite oxidation experiment was done. First, the beaker was put into the ice water bath, then 4 g graphite powder, 2 g $NaNO_3$ (Shanghai Rich Joint Chemical Reagents Co., Ltd.), and 100 mL H_2SO_4 were added, then stirred evenly. 12 g $KMnO_4$ was slowly added to the beaker within 1 h and stirred at 5 °C for 1 h to obtain a dark green solution. Then the beaker was moved to an oil bath and heated at 35 °C for 30 min and stirred all the time. 200 mL ultrapure water was slowly added to the beaker, and then the temperature of the oil bath was raised to about 90 °C for 1 h to obtain a golden yellow suspension. When the temperature was decreased to about 50 °C, 50 mL H_2O_2 (30% in purity, China Sun Specialty Products Co., Ltd.) was added to reduce excess oxidant about 20 min, then cooled down to room temperature.

Because the time required for GO suction filtration was too long, the centrifugation method (5000 rpm, 15 min) was chosen to wash the suspension until the liquid could not be separated by centrifugation. Then it was dialyzed with a dialysis bag (MWco: 8000–14000 Da, Sinopharm Chemical Reagent Co., Ltd.) for three days to remove the impurity ions in the GO. The dialyzed GO was ultrasonically dispersed for 60 min, then centrifuged again (8000 rpm, 15 min), and the upper layer of colloid was freeze-dried to obtain a sponge-like GO.

2.2. Observation of LC

A certain amount of sponge-like GO was dissolved in water to prepare 0.5 wt%, 1 wt% and 2 wt% aqueous solution of GO. The GO was dispersed evenly with the high shear emulsifying machine and ultrasonically treated for 2 h. The obtained GOLC aqueous solution was dropped on a glass slide flattened which was subjected to the observation by crossed polarizers. The GOLC in the obtained solution was transferred to the PDMS, and thermally reduced. The product was observed by crossed polarizers.

2.3. Extractant selection

In order to fully transfer GOLC from the aqueous phase to the organic phase, toluene, n-butyl acetate, cyclohexane, trichloromethane, dichloromethane and diethyl ether as extractant were studied to find the best extractant. Briefly, 10 mL of extractant was mixed with 10 mL GOLC aqueous solution (1 mg/mL) and 120 mg graft copolymer PAPMS-b-PDMS was added, which was stirred on a magnetic stirrer for 2 h to compare the ability of GOLC to be extracted from the aqueous phase to the organic phase. 10 mL of 1 mg/mL GO aqueous solution was prepared, then 10 mL diethyl ether was added. The mass ratio of GO to PAPMS-b-PDMS (2–3 mol% of amine groups) was controlled to be 1:8, 1:10 and 1:12. The solution was mixed on a magnetic stirrer for 2 h, and observed for the extraction efficiency.

2.4. Preparation of reduced graphene oxide liquid crystal (rGOLC) and PDMS composites

First, the diethyl ether solution of GOLC was added into the fume hood to evaporate most of the diethyl ether and then mixed with 10 g hydroxy-terminated PDMS (750 mPa s, Jiangxi Xing Huo Organic Silicone Plant). The diethyl ether was completely removed by heating in an oven at 60 °C for 30 min and then kept at 180 °C for 4 h to thermally reduce GOLC to rGOLC. After cooling, PDMS cross-linking agent and catalyst were added and stirred well. Then, the nanosuspensions were poured into a mold and cross-linked at room temperature to obtain the solid rGOLC/PDMS composites.

2.5. Characterization

The surface microscopic images of GO were observed with a scanning electron microscope (SEM) (JSM-6480, JEOL). The Raman spectra of GO and GO-copolymer were measured by using a Renishaw confocal Raman microprobe (Raman) (InVia, Renishaw), working range was 100–2000 cm^{-1}. The functional groups of GO and GO-copolymer were measured by using a Fourier Transform infrared spectroscopy (FTIR) (Cary, NYSE: A), working range was 400–4000 cm^{-1}. The samples were prepared by KBr pellet method, and the ratio of sample to KBr was 1:200. The crystal states of GO were measured by using an X-Ray Diffractometer (XRD) (XRD-6000, SHIMADZU), scan range 2θ was 10°–80°. The mechanical properties of rGOLC/PDMS composites were measured using an electronic universal testing machine (CMT4430, MTS China). The LC phase of GO and rGO was observed by using a polarizing microscope (50IPOL, Nikon). The dielectric properties of the rGOLC/PDMS composites were measured at room temperature by using an impedance analyzer (Agilent-4294A, Hong Da Electronic Instrument Co., Ltd), working frequency range was 10^{-1}-10^{6} Hz.

3. Results and discussion

This improved Hummers' method can conveniently prepare GO containing many polar groups, which is convenient for mixing with other substances [49,50,57–60]. The FTIR was used to detect those groups (Fig. 1a). For GO, the absorption peak at 3100-3500 cm^{-1} corresponds to the –OH stretching vibration, which is the absorption peak formed by the –OH on the GO sheet. The absorption peak near 1730 cm^{-1} is due to the stretching vibration absorption of C═O in the carboxyl group. The absorption peak near 1630 cm^{-1} is caused by the

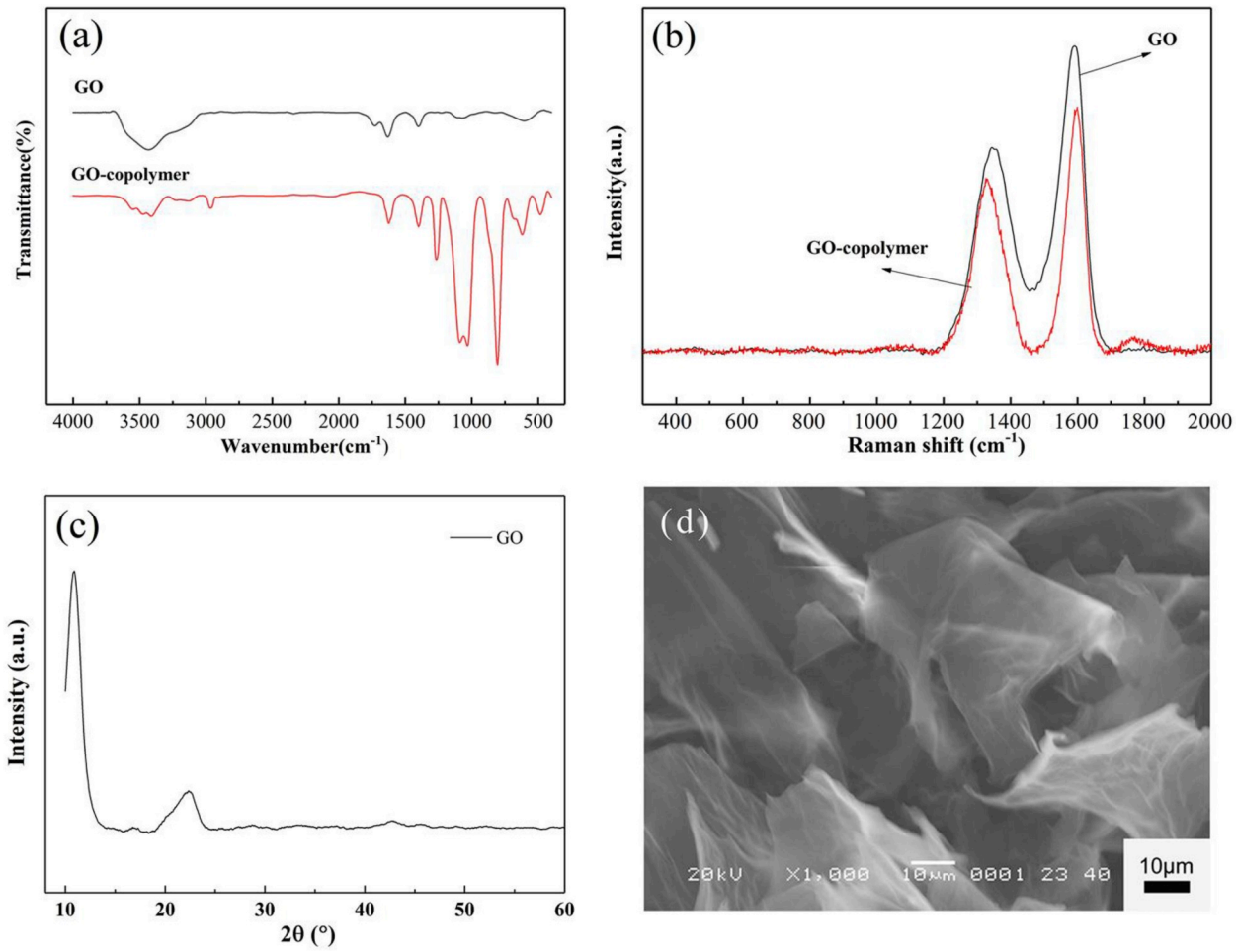

Fig. 1. (a) FTIR spectra of GO and GO-copolymer. GO-copolymer is composed of GO and PAPMS-b-PDMS with 1: 12, (b) Raman spectra of GO and GO-copolymer. (c) XRD patterns of GO. (d) SEM image of GO.

C═C stretching vibration [33,61,62]. The absorption peak near 1400 cm^{-1} is ascribed to the in-plane bending vibration of the C–H group. The absorption peak near 1100 cm^{-1} corresponds to the stretching vibration of the C–O–C group. They indicate that GO contains the oxygen-containing groups. Fig. 1b shows two distinct Raman scattering peaks for GO. One is the D peak at 1350 cm^{-1} and the other is the G peak at 1593 cm^{-1}. The D peak is generated by the vibration of sp^3 hybridized carbon atoms, reflecting the defects of the internal structure of GO. And the G peak is produced by the sp^2 hybrid carbon ring and atomic stretching vibration, representing the symmetry and order degree in the GO molecular structure [63–66]. In the Raman analysis, the intensity ratio of the D peak to the G peak (I_D/I_G) is often used to indicate the disorder degree of the graphite sheet [60,67–69]. The I_D/I_G of GO obtained by the experiment was 0.67. Neither graphene nor graphite had a D peak, indicating that the obtained oxygen-containing group on the GO resulted in the appearance of a D peak of the defect peak [61,66,70].

As can be seen from Fig. 1a, the infrared absorption testing of GO-copolymer shows several new absorption peaks compared to GO, for example, the stretching vibration of the Si–C bond at 810 cm^{-1}, the bending vibration of the Si–C bond at 1256 cm^{-1}, the stretching vibration of the Si–O bond at 1028 cm^{-1} and 1090 cm^{-1}, the stretching vibration of the –CH bond at 2965 cm^{-1}. There are also some absorption peaks overlapping with the absorption peak of GO, which is the N–H bond at 3000 cm^{-1} and the C–N bond at 1400 cm^{-1}. The C═O bond at 1720 cm^{-1} also moves to around 1620 cm^{-1} because of the formation of the amide group. Fig. 1b shows that the I_D/I_G of the GO-copolymer is 0.7, indicating that the PAPMS-b-PDMS copolymer does not change the structure of the GO. It can be seen from FTIR and Raman spectra that GO was successfully grafted with PAPMS-b-PDMS copolymer and its layered structure did not change significantly.

The peak at 2θ of 11° in Fig. 1c is the characteristic peak of GO. In addition, a weak peak at 22° is a characteristic peak of graphite, indicating that some graphite remains in the GO. The residual graphite content is relatively small, and subsequent experiments will be performed by ultrasonic treatment and thermal reduction, so the residual small amount of graphite has little effect on the experiment. Fig. 1d is an SEM image of GO. It can be clearly seen that GO is a single layer or a few layers, and exhibits a stable structure such as bending and wrinkles, indicating that GO has a higher degree of oxidation and a distinct separation of GO sheets.

Since the LC has a birefringence phenomenon, it can be observed under a polarizing microscope. But the isotropic substance cannot be seen under the polarizing microscope because it does not have a birefringence phenomenon [47]. It can be seen from Fig. 2 that when the concentration of GO is 0.5 wt%, the LC was observed only at the edge, and it was hardly observed in the middle portion (Fig. 2a), indicating that only a small amount of LC can be formed. Those LC structures were distributed at the edge of the droplet due to the surface tension. It should be noted that the time for observing the LC should not be too long, otherwise the concentration is no longer the initial concentration. LC phase can be observed in the entire droplet when the concentration of GO reaches 1 wt% (Fig. 2b). The proportion of the LC phase has been reported even reaching 100% [47]. The concentration of GO is 2 wt% in

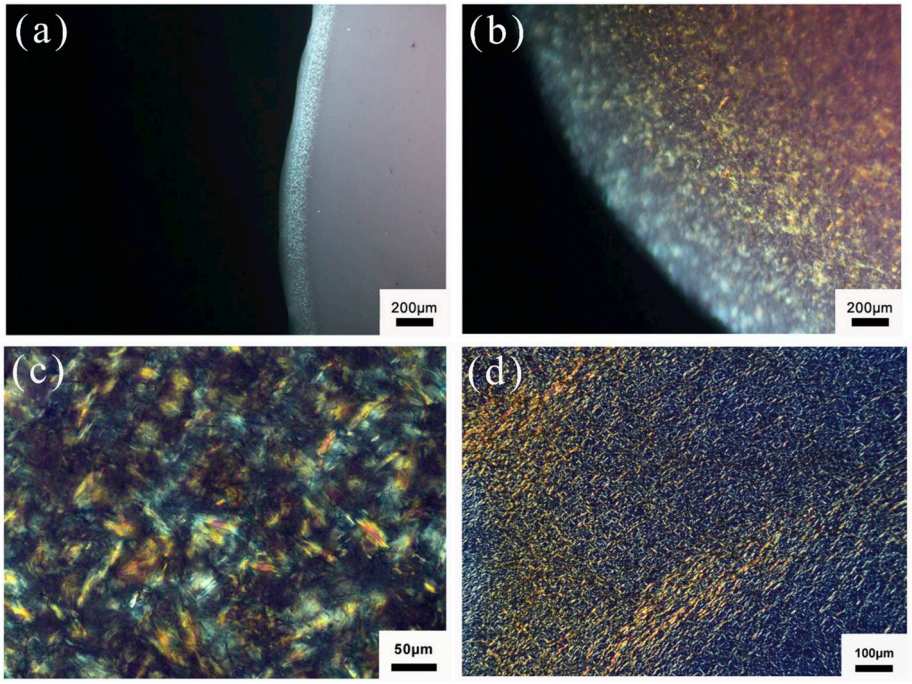

Fig. 2. Optical micrographs with crossed polarizers of GOLC. Different concentrations of GOLC aqueous solution, (a) 0.5 wt%, (b) 1 wt%, (c) 2 wt%, (d) 0.5 wt% after dried, respectively.

Fig. 2c, the LC phase on the graph is elongated and has different angles, reflecting different orientation states of the crystal domains. If an electric field or tensile state is added at this time, the domains can be coaxially oriented, thereby improving the electrical and mechanical properties in this direction [47]. Fig. 2d is optical micrographs with crossed polarizers of the 0.5 wt% aqueous solution of GO after drying. The GO solution was dropped on a glass slide, and then dried at 60 °C to obtain dry GO. It can be seen that the GOLC can maintain the crystal state after drying, so this structure is envisioned to be introduced into the composites.

Fig. 3a is a schematic diagram of the interaction principle between GO and PAPMS-b-PDMS copolymer. The carboxyl group on the GO sheet

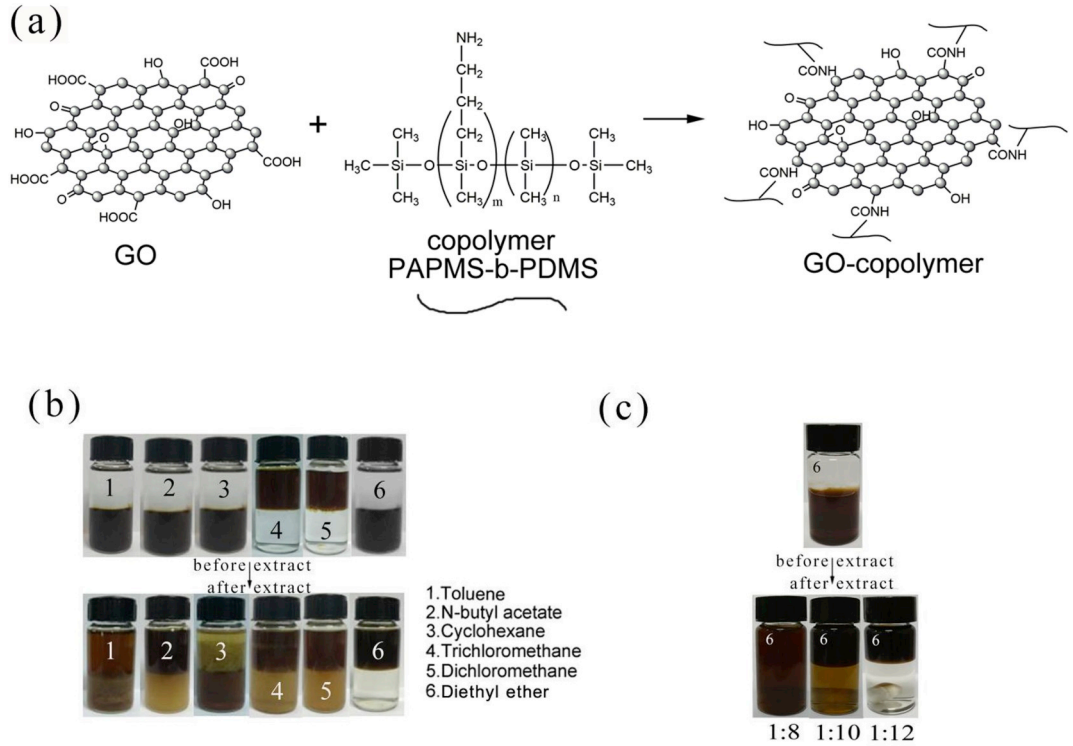

Fig. 3. (a) Schematic diagram of the interaction between GO and PAPMS-b-PDMS (2–3 mol% of amine groups). (b) The GOLC was extracted from the aqueous phase to the oil phase by different extractant. (c) different proportions of PAPMS-b-PDMS copolymer was added for extraction, the phase transfers are shown as the mass ratio of GO to the copolymer. The top layer is a diethyl ether layer.

and the amine group on the PAPMS-b-PDMS copolymer are covalently bonded by their dehydration of the group to make it lipophilic and can be uniformly mixed with an oily substance such as diethyl ether and PDMS. And the copolymer does not destroy the carbon lattice of GO. Fig. 3b shows the extraction efficiency of six organic solvents for the GOLC-copolymer. We can find that only diethyl ether in the same volume of organic solvent can completely extract the GOLC-copolymer. This is because C–O–C in diethyl ether has good compatibility with GOLC-copolymer, and its solubility to GOLC-copolymer is very large, so we use diethyl ether as the extractant.

Diethyl ether is known to have the best extraction effect on GOLC-copolymer. Then proportion of PAPMS-b-PDMS copolymer was further studied to fully functionalize GOLC. Since GOLC is difficult to dissolve in diethyl ether, GOLC was modified to increase its solubility in diethyl ether. Fig. 3c shows the modification effect of GOLC with the copolymer content of 1:8 to 1:12 (GO: copolymer with mass ratio). When the mass ratio was 1:12, GOLC-copolymer could be completely extracted into the upper diethyl ether layer. Therefore, GOLC was functionalize with copolymer by a 1:12 mass ratio was used in subsequent experiments.

Fig. 4a is an optical micrograph with crossed polarizers of GOLC-copolymer dispersed in PDMS with a concentration of 2 wt%. The observed many bright spots distributed evenly in the PDMS means that the GOLC stably present in the polymer. The bubbles in the image are due to the presence of non-volatile diethyl ether (arrow point). Now we know that the aqueous GO solution can form a LC phase, and when the mass fraction of GO reaches a certain value, the proportion of the LC phase almost reaches 100% [47]. Then, the high-temperature in-situ thermal reduction is carried out, and it is desired to obtain the rGO-composites which maintain the LC structure, thereby increasing the electrical properties and mechanical properties of the composites. Fig. 4b shows that GOLC-copolymer and PDMS composite after the thermal reduction at 180 °C for 4 h. Many bright spots can be seen in the image and are the rGOLC formed in PDMS. However, there are some pores/voids left by the evaporation of diethyl ether (arrow point). These defects have a great influence on the material properties. Later, these defects were removed by vacuum. The LC phase of the thermally rGO is uniform in PDMS and can stably present which is because the chemically modified rGOLC prevents agglomeration during heating. Then, the rGOLC-copolymer and the PDMS mixture were cross-linked by adding a crosslinking agent and a catalyst to obtain the desired rGOLC/PDMS composites.

Fig. 4c and d shows the cross-sectional SEM images of rGOLC/PDMS composites. Fig. 4c has some dimple of ductile fracture (arrow point) of PDMS without adding GOLC, which can be concluded that this is only the morphology of polymer ductile fracture. However, for the rGOLC/PDMS composites, besides the ductile fracture, a flaky substance at the crack (arrow point) can be observed, Fig. 4d, which is the layer of rGO by high-temperature reduction of GO. Moreover, the graphene sheets do not show bending and folding, indicating that the graphene sheets in the polymer are arranged in parallel with each other. Therefore, the graphene sheet layer may form a large number of microcapacitors [18–20,29,47].

Fig. 5a shows the mechanical properties of the sample tested by a universal tensile tester. The mechanical properties of the composites increase with increasing the rGOLC content when the added amount of rGOLC is low, this is because rGOLC plays a reinforcing role for PDMS. It is a small-layer structure and has a quantum effect that can greatly improve the mechanical performance of PDMS. The tensile properties of rGOLC/PDMS composites reach the highest value when the rGOLC content is 2 wt%, the tensile strength is 1 MPa, and the elongation at break is 280%. However, the mechanical properties of the composites are decreased when the content of rGOLC is increased to a certain ratio, this is because the viscosity of the mixture is too large, which causes structural defects in PDMS, but it still has better mechanical properties than pure PDMS. Compared with Lee's research [71], we not only increased the doping concentration of GO, but also ensured that GO after thermal reduction still maintains the structure of LC in PDMS, which greatly improves the performance of the composite.

PDMS doped with conductive particles can form a dielectric composite, but conductive paths are often formed before a high permittivity composite is obtained, so the permittivity of this composite is low and the dielectric loss is large. However, a high permittivity composite can be obtained by a conductive-insulated core-shell structure or a conductive LC structure, and its dielectric loss can also be kept at a low

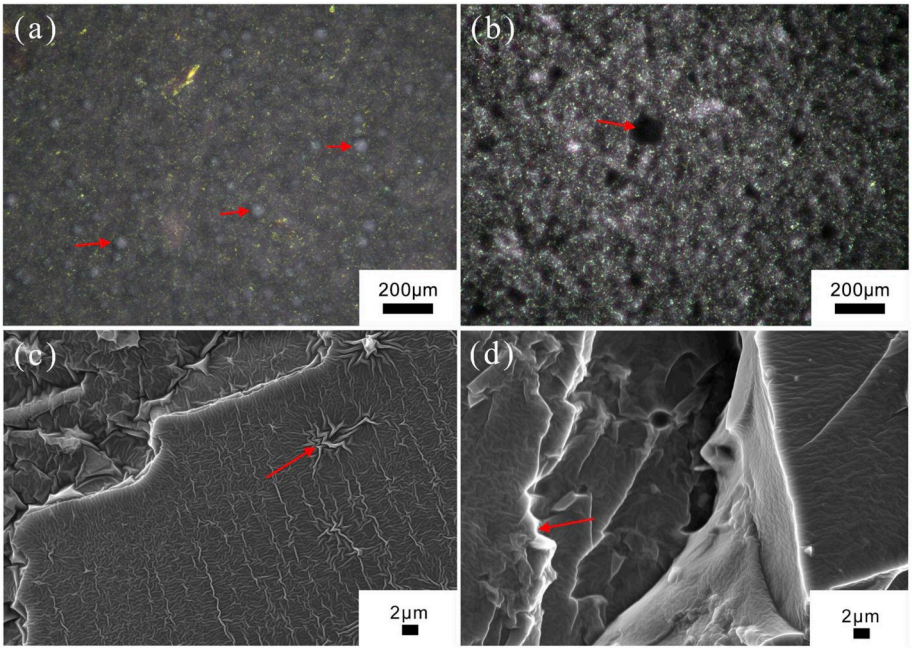

Fig. 4. Optical micrographs with crossed polarizers of GOLC-copolymer dispersed in PDMS. (a) the concentration of 2 wt%. (b) the concentration of 2 wt% after thermal at 180 °C for 4 h. (c) Cross-sectional SEM image with a concentration of 0 wt% for cross-linked PDMS. (d) Cross-sectional SEM image with a concentration of 1 wt% for cross-linked PDMS composites.

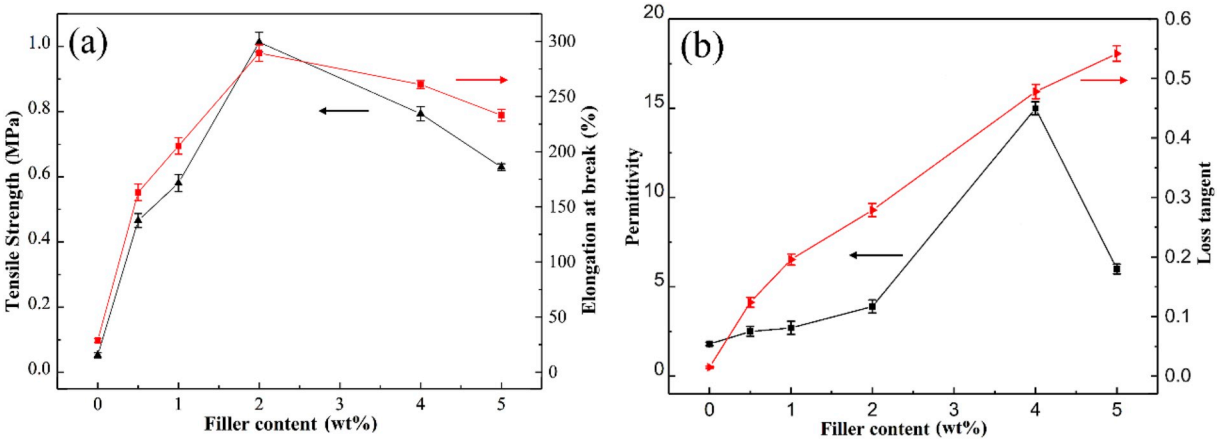

Fig. 5. (a) The mechanical properties of the rGOLC/PDMS composites (b) Permittivity and loss tangent of rGOLC/PDMS composites at 1 kHz.

Table 1
Effect of Different Fillers on Dielectric Properties of PDMS, test frequency is 1 kHz.

PDMS composites	Dielectric constant Pure/Modified PDMS		Increase (%)	Dielectric loss tangent	Concentration	Ref
RGO	3.1	89.5	2800	1.5	2 wt%	[72]
RGO	3.4	9.6	280	0.41	0.5 vol%	[73]
RGOLC	1.8	15	800	0.47	4 wt%	–
$PbZr_{0.52}Ti_{0.48}O_3$	3.8	8.6	220	0.27	41.2 wt%	[74]
$CaCu_3Ti_4O_{12}$	3.13	5.45	170	0.0025	8.4 vol%	[75]
Montmorillonite	NA	3.1	NA	0.17	8 wt%	[76]
TiO_2	2.9	3.2	110	0.05	5 wt%	[77]
Ag@SiO2 nanoparticles	3	21	700	0.03	31 vol%	[78]

level. Some typical dielectric composites and dielectric properties are shown in Table 1. For instance, the composite formed by PDMS doped normal RGO has a relatively low permittivity [72,73]. If the RGO content is increased, the dielectric loss tangent is rapidly increased to 1.5 [72], so such materials are not suitable as high permittivity materials. However, when the filler is rGOLC or CCTO@MWCNT [29,79], the permittivity of the composite increases several hundred times compared to pure PDMS, and the dielectric loss tangent remains at a low level. Therefore, rGOLC composites can provide a direction for the fabrication of high permittivity materials.

It can be seen from Fig. 5b that the permittivity of the composites increases gradually with the increase of the rGOLC filling amount. The

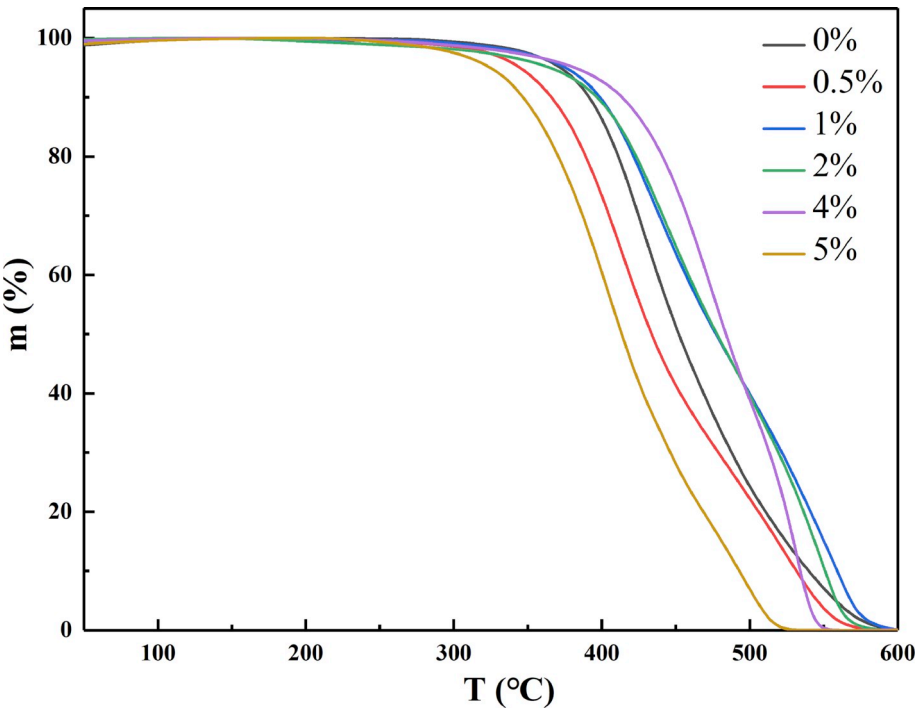

Fig. 6. Thermogravimetric Analysis of Graphene/polydimethylsiloxane nanocomposites.

permittivity increases only from 1.8 to 3.9 when the filler content is less than 2 wt%. But when the filler content is increased to 4 wt%, the permittivity sharply reaches a maximum of 15, the permittivity is increased by 800% compared to pure PDMS. When a small amount of rGOLC as polarized particles is added in PDMS, the rGOLC sheets are uniformly dispersed in the polymer, and the sheets are far apart. The few polarized particles cause the low permittivity in the composites. However, as the rGOLC content increases, the distance of the rGOLC sheets in the composites gradually decreases that especially promotes the displacement polarization in an electric field to form the micro-capacitors, so the permittivity is greatly improved in the macroscopic range. However, the dielectric constant does not obviously increase without limit with the increase of the filler content. When the filler is increased to 5 wt%, the graphene sheets will contact each other to generate a leakage current, thereby causing the permittivity to start to decrease. This is consistent with Yuan's experimental results [80].

For the dielectric loss, it displays a similar tendency to the permittivity. As shown in Fig. 5b, with increasing the rGOLC content, the dielectric loss is also raised. The dielectric loss is the ratio of the conductance to the capacitance. However, polarization raises the permittivity which usually accompanies an increasing dielectric loss. As the filler content increases, they will contact each other and many conductive paths will occur, which means energy loss. The lost electric energy is released through thermal energy. Fortunately, for the rGOLC/PDMS, it becomes difficult to form a conductive path since rGO forms a LC phase in the composites, even if the content of the filler is large. Therefore, the loss dissipation factor of the rGOLC composites is smaller than that of the amorphous composite, and its loss tangent at 1 kHz is only 0.47 when the filler content is 4 wt%.

The Thermogravimetric analysis test was carried out to characterize the thermal stability of rGOLC/PDMS nanocomposites. It can be seen from Fig. 6 that as the content of rGOLC increases, the thermal stability of rGOLC/PDMS nanocomposites first increases and then decreases. This is because when the filler content is large, too many defects are generated, and the rGOLC not only does not enhance, but reduces the thermal stability of the material. When the filler content is 4 wt%, the nanocomposites have the best thermal stability, which is consistent with the trend of dielectric constant. In addition, the rGOLC/PDMS nanocomposites are rarely degrade at 400 °C, which provides a solution for use under extreme conditions.

4. Conclusion

In summary, rGOLC/PDMS composites obtained by high-temperature reduce GOLC in the PDMS matrix. Since rGOLC obtained by thermal reduction still has LC state, rGOLC sheets tend to be arranged in parallel in the polymer, resulting in composites with good dielectric properties and high mechanical properties. The permittivity of the composites increases to maximum 15 when the filler concentration reaches 4 wt%. The permittivity increases by 800% compared to pure PDMS. Therefore, the potential of rGOLC/PDMS composites in the field of dielectric materials is enormous. These rGOLC sheets can combine with other polymers [6,81–85] for preparing other functional structural nanocomposites with many other applications like electromagnetic interference (EMI) shielding [86–89], sensing [90,91], etc.

Conflicts of interest

The authors declare no conflict of interest.

References

[1] Liu M, Li B, Zhou H, Chen C, Liu Y, Liu T. Extraordinary rate capability achieved by a 3D "skeleton/skin" carbon aerogel–polyaniline hybrid with vertically aligned pores. Chem Commun 2017;53(19):2810–3.

[2] Gu H, Xu X, Cai j, Wei S, Wei H, Liu H, et al. Controllable organic magnetoresistance in polyaniline coated poly(p-phenylene-2,6-benzobisoxazole) short fibers. Chem Commun 2019. https://doi.org/10.1039/C9CC04789A. In press.

[3] Zhang Y, An Y, Wu L, Chen H, Li Z, Dou H, et al. Metal-free energy storage systems: combining batteries with capacitors based on methylene blue functionalized graphene cathode. J Mater Chem A 2019. https://doi.org/10.1039/C9TA06734E. In press.

[4] Zhu G, Cui X, Zhang Y, Chen S, Dong M, Liu H, et al. Poly (vinyl butyral)/graphene oxide/poly (methylhydrosiloxane) nanocomposite coating for improved aluminum alloy anticorrosion. Polymer 2019;172:415–22.

[5] Gu H, Xu X, Dong M, Xie P, Shao Q, Fan R, et al. Carbon nanospheres induced high negative permittivity in nanosilver-polydopamine metacomposites. Carbon 2019;147:550–8.

[6] Ma Y, Hou C, Zhang H, Zhang Q, Liu H, Wu S, et al. Three-dimensional core-shell Fe3O4/polyaniline coaxial heterogeneous nanonets: preparation and high performance supercapacitor electrodes. Electrochim Acta 2019;315:114–23.

[7] Cheng CB, Fan RH, Fan GH, Liu H, Zhang JX, Shen JX, et al. Tunable negative permittivity and magnetic performance of yttrium iron garnet/polypyrrole metacomposites at the rf frequency. J Mater Chem C 2019;7(11):3160–7.

[8] Liang T, Qi L, Ma Z, Xiao Z, Wang Y, Liu H, et al. Experimental study on thermal expansion coefficient of composite multi-layered flaky gun propellants. Composites Part B 2019;166:428–35.

[9] Wang C, Murugadoss V, Kong J, He Z, Mai X, Shao Q, et al. Overview of carbon nanostructures and nanocomposites for electromagnetic wave shielding. Carbon 2018;140:696–733.

[10] Wei H, Wang H, Xia Y, Cui D, Shi Y, Dong M, et al. An overview of lead-free piezoelectric materials and devices. J Mater Chem C 2018;6(46):12446–67.

[11] Sun K, Fan RH, Zhang XH, Zhang ZD, Shi ZC, Wang N, et al. An overview of metamaterials and their achievements in wireless power transfer. J Mater Chem C 2018;6(12):2925–43.

[12] Liu H, Li Q, Zhang S, Yin R, Liu X, He Y, et al. Electrically conductive polymer composites for smart flexible strain sensors: a critical review. J Mater Chem C 2018;6(45):12121–41.

[13] Li Q, Liu H, Zhang S, Zhang D, Liu X, He Y, et al. Superhydrophobic electrically conductive paper for ultrasensitive strain sensor with excellent anticorrosion and self-cleaning property. ACS Appl Mater Interfaces 2019;11(24):21904–14.

[14] Ma L, Zhu Y, Wang M, Yang X, Song G, Huang Y. Enhancing interfacial strength of epoxy resin composites via evolving hyperbranched amino-terminated poss on carbon fiber surface. Compos Sci Technol 2019;170:148–56.

[15] Ma L, Li N, Wu G, Song G, Li X, Han P, et al. Interfacial enhancement of carbon fiber composites by growing TiO2 nanowires onto amine-based functionalized carbon fiber surface in supercritical water. Appl Surf Sci 2018;433:560–7.

[16] Ma L, Zhu Y, Feng P, Song G, Huang Y, Liu H, et al. Reinforcing carbon fiber epoxy composites with triazine derivatives functionalized graphene oxide modified sizing agent. Composites Part B 2019;176:107078.

[17] Guo YQ, Ruan KP, Yang XT, Ma TB, Kong J, Wu NN, et al. Constructing fully carbon-based fillers with a hierarchical structure to fabricate highly thermally conductive polyimide nanocomposites. J Mater Chem C 2019;7(23):7035–44.

[18] Dang Z, Yuan J, Zha J, Zhou T, Li S, Hu G. Fundamentals, processes and applications of high-permittivity polymer–matrix composites. Prog Mater Sci 2012;57(4):660–723.

[19] Dang ZM, Yuan JK, Yao SH, Liao RJ. Flexible nanodielectric materials with high permittivity for power energy storage. Adv Mater 2013;25(44):6334–65.

[20] Nan CW, Shen Y, Ma J. Physical properties of composites near percolation. Annu Rev Mater Res 2010;40(1):131–51.

[21] Luo XL, Pei F, Wang W, Qian HM, Miao KK, Pan Z, et al. Microwave synthesis of hierarchical porous materials with various structures by controllable desilication and recrystallization. Microporous Mesoporous Mater 2018;262:148–53.

[22] Zhao Z, Bai P, Misra RDK, Dong M, Guan R, Li Y, et al. Alsi10mg alloy nanocomposites reinforced with aluminum-coated graphene: selective laser melting, interfacial microstructure and property analysis. J Alloy Comp 2019;792:203–14.

[23] Zhao Y, Zhang B, Hou H, Chen W, Wang M. Phase-field simulation for the evolution of solid/liquid interface front in directional solidification process. J Mater Sci Technol 2019;35(6):1044–52.

[24] Zhao Y, Qi L, Jin Y, Wang K, Tian J, Han P. The structural, elastic, electronic properties and debye temperature of d022-ni3v under pressure from first-principles. J Alloy Comp 2015;647:1104–10.

[25] Zhao Y, Tian X, Zhao B, Sun Y, Guo H, Dong M, et al. Precipitation sequence of middle al concentration alloy using the inversion algorithm and microscopic phase field model. Sci Adv Mater 2018;10(12):1793–804.

[26] Barcohen Y. Electroactive polymers as artificial muscles: a review. J Spacecr Rocket 2002;39(6):822–7.

[27] Han X, Chen S, Lv X, Luo H, Zhang D, Bowen CR. Using a novel rigid-fluoride polymer to control the interfacial thickness of graphene and tailor the dielectric behavior of poly(vinylidene fluoride-trifluoroethylene-chlorotrifluoroethylene) nanocomposites. Phys Chem Chem Phys 2018;20(4):2826–37.

[28] Shen C, Liu X, Cao H, Zhou Y, Liu J, Tang J, et al. Brain-like navigation scheme based on mems-ins and place recognition. Appl Sci 2019;9(8):1708.

[29] Yuan J, Luna A, Neri W, Zakri C, Schilling T, Colin A, et al. Graphene liquid crystal retarded percolation for new high-k materials. Nat Commun 2015;6(8700). 8700-8700.

[30] Novoselov KS, Geim AK, Morozov SV, Jiang D, Zhang Y, Dubonos SV, et al. Electric field effect in atomically thin carbon films. Science 2004;306(5696):666–9.

[31] Hecht DS, Hu L, Irvin G. Emerging transparent electrodes based on thin films of carbon nanotubes, graphene, and metallic nanostructures. Adv Mater 2011;23(13):1482–513.

[32] Yu X, Cheng H, Zhang M, Zhao Y, Qu L, Shi G. Graphene-based smart materials. Nat Rev Mater 2017;2(9):17046.
[33] Jiao Y, Zhang J, Liu S, Liang Y, Li S, Zhou H, et al. The graphene oxide ionic solvent-free nanofluids and their battery performances. Sci Adv Mater 2018;10(12):1706–13.
[34] Liu M, Meng Q, Yang Z, Zhao X, Liu T. Ultra-long-term cycling stability of an integrated carbon–sulfur membrane with dual shuttle-inhibiting layers of graphene "nets" and a porous carbon skin. Chem Commun 2018;54(40):5090–3.
[35] Liu M, Yang Z, Sun H, Lai C, Zhao X, Peng H, Liu T. A hybrid carbon aerogel with both aligned and interconnected pores as interlayer for high-performance lithium–sulfur batteries. Nano Res 2016;9(12):3735–46.
[36] Han NM, Wang Z, Shen X, Wu Y, Liu X, Zheng Q, et al. ACS Appl Mater Interfaces 2018;10(7):6580–92.
[37] Nassira H, Sanchez Ferrer A, Adamcik J, Handschin S, Mahdavi H, Taheri Qazvini N, et al. Gelatin-graphene nanocomposites with ultralow electrical percolation threshold. Adv Mater 2016;28(32):6914–20.
[38] Nistal A, Garcia E, Pérez Coll D, Prieto C, Belmonte M, Osendi MI, et al. Low percolation threshold in highly conducting graphene nanoplatelets/glass composite coatings. Carbon 2018;139:556–63.
[39] Xi J, Liu Y, Wu Y, Hu J, Gao W, Zhou E, et al. Multifunctional bicontinuous composite foams with ultralow percolation thresholds. ACS Appl Mater Interfaces 2018;10(24):20806–15.
[40] Zhao F, Zhang G, Zhao S, Cui J, Gao A, Yan Y. Fabrication of pristine graphene-based conductive polystyrene composites towards high performance and light-weight. Compos Sci Technol 2018;159:232–9.
[41] Behabtu N, Lomeda JR, Green MJ, Higginbotham AL, Sinitskii A, Kosynkin DV, et al. Spontaneous high-concentration dispersions and liquid crystals of graphene. Nat Nanotechnol 2010;5(6):406–11.
[42] Zamoraledezma C, Puech N, Zakri C, Grelet E, Moulton SE, Wallace GG, et al. Liquid crystallinity and dimensions of surfactant-stabilized sheets of reduced graphene oxide. J Phys Chem Lett 2012;3(17):2425–30.
[43] Li D, Muller MB, Gilje S, Kaner RB, Wallace GG. Processable aqueous dispersions of graphene nanosheets. Nat Nanotechnol 2008;3(2):101–5.
[44] Xu Z, Gao C. Aqueous liquid crystals of graphene oxide. ACS Nano 2011;5(4):2908–15.
[45] Schilling T, Dorosz S, Radu M, Mathew M, Jungblut S, Binder K. Mixtures of anisotropic and spherical colloids: phase behavior, confinement, percolation phenomena and kinetics. Eur Phys J Spec Top 2013;222(11):3039–52.
[46] Mathew M, Schilling T, Oettel M. Connectivity percolation in suspensions of hard platelets. Phys Rev E 2012;85(061407):061407.
[47] Kim JE, Han TH, Lee SH, Kim JY, Ahn CW, Yun JM, Kim SO. Graphene oxide liquid crystals. Angew Chem Int Ed Engl 2011;50(13):3043–7.
[48] Padmajan Sasikala S, Lim J, Kim IH, Jung HJ, Yun T, Han TH, et al. Graphene oxide liquid crystals: a frontier 2D soft material for graphene-based functional materials. Chem Soc Rev 2018;47(16):6013–45.
[49] Guo Y, Xu G, Yang X, Ruan K, Ma T, Zhang Q, et al. Significantly enhanced and precisely modeled thermal conductivity in polyimide nanocomposites with chemically modified graphene via in situ polymerization and electrospinning-hot press technology. J Mater Chem C 2018;6(12):3004–15.
[50] Zhang J, Liang Y, Wang X, Zhou H, Li S, Zhang J, et al. Strengthened epoxy resin with hyperbranched polyamine-ester anchored graphene oxide via novel phase transfer approach. Adv Compos Hybrid Mater 2018;1(2):300–9.
[51] Pei S, Cheng H. The reduction of graphene oxide. Carbon 2012;50(9):3210–28.
[52] Valles C, Nunez JD, Benito AM, Maser WK. Flexible conductive graphene paper obtained by direct and gentle annealing of graphene oxide paper. Carbon 2012;50(3):835–44.
[53] Bagri A, Mattevi C, Acik M, Chabal YJ, Chhowalla M, Shenoy VB. Structural evolution during the reduction of chemically derived graphene oxide. Nat Chem 2010;2(7):581–7.
[54] Li T, Pickel AD, Yao Y, Chen Y, Zeng Y, Lacey SD, et al. Thermoelectric properties and performance of flexible reduced graphene oxide films up to 3,000 k. Nat Energy 2018;3(2):148–56.
[55] Luo D, Zhang G, Liu J, Sun X. Evaluation criteria for reduced graphene oxide. J Phys Chem C 2011;115(23):11327–35.
[56] Hummers SW, Offeman RE. Preparation of graphitic oxide. J Am Chem Soc 1958;80(6). 1339-1339.
[57] Liu H, Dong M, Huang W, Gao J, Dai K, Guo J, et al. Lightweight conductive graphene/thermoplastic polyurethane foams with ultrahigh compressibility for piezoresistive sensing. J Mater Chem C 2017;5(1):73–83.
[58] Tang J, Zhou H, Liang Y, Shi X, Yang X, Zhang J. Properties of graphene oxide/epoxy resin composites. J Nanomater 2014:175. 2014.
[59] Wang C, Zhao M, Li J, Yu J, Sun S, Ge S, et al. Silver nanoparticles/graphene oxide decorated carbon fiber synergistic reinforcement in epoxy-based composites. Polymer 2017;131:263–71.
[60] Wang X, Liu X, Yuan H, Liu H, Liu C, Li T, et al. Non-covalently functionalized graphene strengthened poly(vinyl alcohol). Mater Des 2018;139:372–9.
[61] Marcano DC, Kosynkin DV, Berlin JM, Sinitskii A, Sun Z, Slesarev A, et al. Improved synthesis of graphene oxide. ACS Nano 2010;4(8):4806–14.
[62] Guo Z, Qian Y, Yuan Y, Wang H, Liu H, Zhang J, et al. Highly efficient uranium adsorption by salicylaldoxime/polydopamine graphene oxide nanocomposites. J Mater Chem 2018;6(48):24676–85.
[63] Eda G, Fanchini G, Chhowalla M. Large-area ultrathin films of reduced graphene oxide as a transparent and flexible electronic material. Nat Nanotechnol 2008;3(5):270–4.
[64] Idrees M, Batool S, Kong J, Zhuang Q, Liu H, Shao Q, et al. Polyborosilazane derived ceramics-nitrogen sulfur dual doped graphene nanocomposite anode for enhanced lithium ion batteries. Electrochim Acta 2019;296:925–37.
[65] Wang Z, Wei R, Gu J, Liu H, Liu C, Luo C, et al. Highly compressible and fire-retardant graphene aerogel with self-adjustable electromagnetic wave absorption. Carbon 2018;139:1126–35.
[66] Kudin KN, Ozbas B, Schniepp HC, Prudhomme RK, Aksay IA, Car R. Raman spectra of graphite oxide and functionalized graphene sheets. Nano Lett 2008;8(1):36–41.
[67] Kirubasankar B, Murugadoss V, Lin J, Ding T, Dong M, Liu H, et al. In situ grown nickel selenide on graphene nanohybrid electrodes for high energy density asymmetric supercapacitors. Nanoscale 2018;10(43):20414–25.
[68] Luo C, Jiao T, Gu J, Tang Y, Kong J. Graphene shield by sibcn ceramic: a promising high-temperature electromagnetic wave-absorbing material with oxidation resistance. ACS Appl Mater Interfaces 2018;10(45):39307–18.
[69] Zhang J, Li P, Zhang Z, Wang X, Tang J, Liu H, et al. Solvent-free graphene liquids: promising candidates for lubricants without the base oil. J Colloid Interface Sci 2019;542:159–67.
[70] Deng W, Kang T, Liu H, Zhang J, Wang N, Lu N, et al. Potassium hydroxide activated and nitrogen doped graphene with enhanced supercapacitive behavior. Sci Adv Mater 2018;10(7):937–49.
[71] Lee KE, Oh JJ, Yun T, Kim SO. Liquid crystallinity driven highly aligned large graphene oxide composites. J Solid State Chem 2015;224:115–9.
[72] Tian M, Wei Z, Zan X, Zhang L, Zhang J, Ma Q, et al. Thermally expanded graphene nanoplates/polydimethylsiloxane composites with high dielectric constant, low dielectric loss and improved actuated strain. Compos Sci Technol 2014;99:37–44.
[73] Panahi-Sarmad M, Razzaghi-Kashani M. Actuation behavior of PDMS dielectric elastomer composites containing optimized graphene oxide. Smart Mater Struct 2018;27(8):085021.
[74] Nayak S, Khastgir D. Polydimethylsiloxane–PbZr0.52Ti0.48O3 nanocomposites with high permittivity: effect of poling and temperature on dielectric properties. J Appl Polym Sci 2019;136(14):47307.
[75] Romasanta LJ, Leret P, Casaban L, Hernández M, de la Rubia MA, Fernández JF, Kenny JM, Lopez-Manchado MA, Verdejo R. Towards materials with enhanced electro-mechanical response: CaCu3Ti4O12–polydimethylsiloxane composites. J Mater Chem 2012;22(47):24705.
[76] Kuznetsov NM, Shevchenko VG, Stolyarova DY, Ozerin SA, Belousov SI, Chvalun SN. Dielectric properties of modified montmorillonites suspensions in polydimethylsiloxane. J Appl Polym Sci 2018;135(32):46614.
[77] Vaimakis-Tsogkas DT, Bekas DG, Giannakopoulou T, Todorova N, Paipetis AS, Barkoula NM. Effect of TiO2 addition/coating on the performance of polydimethylsiloxane-based silicone elastomers for outdoor applications. Mater Chem Phys 2019;223:366–73.
[78] Quinsaat JEQ, Alexandru M, Nüesch FA, Hofmann H, Borgschulte A, Opris DM. Highly stretchable dielectric elastomer composites containing high volume fractions of silver nanoparticles. J Mater Chem A 2015;3(28):14675–85.
[79] Liu G, Chen Y, Gong M, Liu X, Cui Z-K, Pei Q, et al. Enhanced dielectric performance of PDMS-based three-phase percolative nanocomposite films incorporating a high dielectric constant ceramic and conductive multi-walled carbon nanotubes. J Mater Chem C 2018;6(40):10829–37.
[80] Yuan J, Luna A, Neri W, Zakri C, Colin A, Poulin P. Giant electrostriction of soft nanocomposites based on liquid crystalline graphene. ACS Nano 2018;12(2):1688–95.
[81] Yang J, Yang W, Wang X, Dong M, Liu H, Wujcik EK, et al. Synergistically toughening polyoxymethylene by methyl methacrylate–butadiene–styrene copolymer and thermoplastic polyurethane. Macromol Chem Phys 2019;220:1800567.
[82] Berndt AJ, Hwang J, Islam MD, Sihn A, Urbas AM, Ku Z, et al. Poly(sulfur-random-(1,3-diisopropenylbenzene)) based mid-wavelength infrared polarizer: optical property experimental and theoretical analysis. Polymer 2019;176:118–26.
[83] Shi ZJ, Xu GF, Deng J, Dong MY, Murugadoss V, Liu CT, Shao Q, Wu SD, Guo ZH. Structural characterization of lignin from d. Sinicus by ftir and nmr techniques. Green Chem Lett Rev 2019;12(3):235–43.
[84] Xu G, Shi Z, Zhao Y, Deng J, Dong M, Liu C, Murugadoss V, Mai X, Guo Z. Structural characterization of lignin and its carbohydrate complexes isolated from bamboo (dendrocalamus sinicus). Int J Biol Macromol 2019;126:376–84.
[85] Shi Z, Jia C, Wang D, Deng J, Xu G, Wu C, et al. Synthesis and characterization of porous tree gum grafted copolymer derived from prunus cerasifera gum polysaccharide. Int J Biol Macromol 2019;133:964–70.
[86] Jiang D, Murugadoss V, Wang Y, Lin J, Ding T, Wang Z, Shao Q, Wang C, Liu H, Lu N, Wei R, Subramania A, Guo Z. Electromagnetic interference shielding polymers and nanocomposites - a review. Polym Rev 2019;59(2):280–337.
[87] Wu N, Liu C, Xu D, Liu J, Liu W, Liu H, Zhang J, Xie W, Guo Z. Ultrathin high-performance electromagnetic wave absorbers with facilely fabricated hierarchical porous Co/C crabapples. J Mater Chem C 2019;7(6):1659–69.
[88] Chen LX, Zhao J, Wang L, Peng F, Liu H, Zhang JX, Gu JW, Guo ZH. In-situ pyrolyzed polymethylsilsesquioxane multi-walled carbon nanotubes derived ceramic nanocomposites for electromagnetic wave absorption. Ceram Int 2019;45(9):11756–64.
[89] Wu Z, Cui H, Chen L, Jiang D, Weng L, Ma Y, Li X, Zhang X, Liu H, Wang N, Zhang J, Ma Y, Zhang M, Huang Y, Guo Z. Interfacially reinforced unsaturated

polyester carbon fiber composites with a vinyl ester-carbon nanotubes sizing agent. Compos Sci Technol 2018;164:195–203.

[90] Gu H, Zhang H, Ma C, Sun H, Liu C, Dai K, Zhang J, Wei R, Ding T, Guo Z. Smart strain sensing organic–inorganic hybrid hydrogels with nano barium ferrite as the cross-linker. J Mater Chem C 2019;7(8):2353–60.

[91] Jiang D, Wang Y, Li B, Sun C, Wu Z, Yan H, et al. Flexible sandwich structural strain sensor based on silver nanowires decorated with self-healing substrate. Macromol Mater Eng 2019;304(7):1900074.